Optimization of the cross-correlation algorithm for two-component wind field estimation from single aerosol lidar data and comparison with Doppler lidar

Masaki Hamada, Pierre Dérian, Christopher F. Mauzey, and Shane D. Mayor *

California State University, Chico, California

**Corresponding author address:* California State University, Chico, 400 W. First St., Chico, CA 95928

E-mail: sdmayor@csuchico.edu

ABSTRACT

A cross-correlation algorithm optimized for application to horizontally-scanning elastic backscatter lidar data is presented. The performance of the algorithm was tested using synthetic and real data. Experiments where conducted at 100 m AGL during convective conditions over land. Results show that an iterative approach that dynamically reduces the block size provides the largest performance gains. Comparisons with Doppler lidar data indicate excellent agreement for the 10-minute mean wind velocity computed over a set of 150 hours, with R^2 correlation coefficients above 0.99 for each of the two wind components.

1. Introduction

The cross-correlation algorithm is a mainstay in the field of motion estimation. It is used to compute the apparent motion of objects and fluid flows in the fields of robotics, navigation, medical imaging, and geosciences (Murray et al. 2009; Emery et al. 2003; Avants et al. 2008; Schubert et al. 2013; Adrian and Westerweel 2011; Cheng et al. 2005; Antoine et al. 2013). In the atmospheric sciences, the cross-correlation algorithm has been applied to satellite imagery (Leese et al. 1971), radar data (Rinehart and Garvey 1978), and lidar data (Eloranta et al. 1975; Shimizu et al. 1981; Kolev et al. 1988). Under the primary assumption that macroscopic aerosol features are advected by the wind, the wind velocity can be approximated from the apparent motion of these features. Herein, synthetic data and real data are used to confirm the necessary sequence of steps for optimal retrieval of vector flow fields from image sequences made by scanning elastic backscatter lidar.

The cross-correlation algorithm involves computing a cross-correlation function from a pair of images. The peak location of the cross-correlation function indicates the predominant displacement of image features. An inherent characteristic of selecting a single peak is the loss of information that describes the true velocity field that causes the motion of features. If the velocity field is perfectly uniform and no features enter or leave the given interrogation window, the peak location of the cross-correlation function correctly represents the displacement of image features caused by the velocity field. However, perfectly uniform flow fields almost never occur in nature. In the case of non-uniform flow, loss of information is inevitable by selecting a single peak of the cross-correlation function. As shown by Hamada (2014), the performance of the cross-correlation algorithm decreases as non-uniformity of the flow field increases. Currently, very few technologies enable the observation of two-component vector wind fields in the atmosphere. Dual-Doppler is one possibility (Stawiarski et al. 2013). As an alternative, we use the aerosol lidar and estimate the wind velocity field by applying the cross-correlation algorithm to pairs of elastic backscatter images. The lidar system used for this study is the Raman-shifted Eye-safe Aerosol Lidar (REAL) (Mayor and Spuler 2004; Mayor et al. 2005, 2007). A single compact Doppler lidar was used to validate the wind velocity fields resulting from the optimized cross-correlation algorithm applied to the REAL aerosol backscatter images.

The cross-correlation approach has been a primary numerical method for determining fluid motion in particle image velocimetry (PIV) experiments.[1] In most PIV experiments, the fluid is deliberately seeded with very small particles that serve as robust tracers of the local flow. The particles are typically illuminated with a laser light plane and individual particles are discernible in the rapidly collected sequence of images taken by a camera. The particles do not change appreciably in shape nor brightness as they move. For low and moderate particle density experiments, in which the fluid between the particles is dark and does not contribute any information, the motion of the small particles is solely relied upon for determining the motion field. As a result, the cross-correlation functions for PIV experiments contain sharp peaks. Furthermore, it is unlikely that particles straddle the edges of the interrogation window. Particles that appear or disappear within the time between two frames, either by moving into or out of the interrogation window, or into or out of the illumination plane, only contribute to incoherent variance confined to the zero lag of the correlation function.

The application of the cross-correlation approach to derive air motion from atmospheric aerosol backscatter lidar images raises a set of issues that are not present in most PIV experiments (at least low-density experiments). These issues result from the time required for the lidar to collect a scan, the inability to discern individual particles, and the continuous range-dependent presence of image

[1]Recently, optical flow methods have become an alternative. For example, Corpetti et al. (2006) applies an optical-flow scheme to study plane turbulent mixing layer, wake of a circular cylinder, and vorticity measurement.

intensity that is a proxy to particle concentration. In addition, temporally and spatially variable sources of particulate matter and changing atmospheric conditions (stability, humidity, flow speed and direction) pose additional challenges for the approach.

The objective of this paper is to describe the sequence of numerical steps necessary for optimal retrieval of vector motion fields from sequences of scanning elastic backscatter lidar images when using the cross-correlation approach to motion estimation. The goal is to confirm or eliminate previously suggested steps, or add new steps, in order for the algorithm to obtain the set of motion vectors that most closely approximate the vector wind field. In general, the cross-correlation motion estimate is accomplished in a series of several different image processing and numerical steps that collectively make up an algorithm. This paper shows that the unique nature of lidar data influences the choices made regarding what steps should be included when applying to lidar data.

Mayor et al. (2012) compared the results of a cross-correlation algorithm applied to scanning elastic backscatter aerosol lidar data to tower-mounted sonic anemometer wind measurements between 10 and 30 m AGL. The study shows that use of the cross-correlation algorithm for subsets of the full lidar scan that were 500 m $\times$ 500 m and smaller produced noisy results. However, a large and important part of the spectrum of atmospheric motions exist at these microscales. Thus, a higher spatial resolution of the wind velocity fields is desired. The algorithm used by Mayor et al. (2012) was functional but not optimal. It did not include the following steps: (1) the zero-padding to account for non-periodic images; (2) the Tukey window to reduce the undesirable effects of aerosol features entering and leaving the block area; (3) the multi-pass interrogation for iterative refinement of the motion estimation; (4) the multi-grid interrogation to improve the spatial resolution of the resulting flow fields; and (5) deforming the scan images to correct for the mean advection of aerosol features during the time required to complete one scan, as described by Sasano et al. (1982). According to Hamada (2014), which used synthetic lidar backscatter images and wind fields, the performance of the cross-correlation algorithm is increased by steps (1), (2), and (3). In addition, step (4) is necessary to improve the spatial resolution of the motion estimation. Furthermore, step (5) is needed to prevent velocity biases associated with image distortion due to the time for completing scans. Thus, the hypothesis of this paper is that the wind velocity estimation from elastic lidar backscatter images is optimized by the 5 steps described above.

This paper is organized as follows: Section 2 introduces the cross-correlation algorithm and describes the options that improve the wind velocity estimation. In Section 3, the performance of the cross-correlation algorithm with these options is evaluated by using synthetic lidar backscatter images and wind velocity fields. In Section 4, the performance of the optimized cross-correlation algorithm is validated by field experiments using the Doppler lidar (DL) as a reference.

2. Application of the cross-correlation algorithm to elastic lidar backscatter images

Scanning lidar data are collected in a spherical system with coordinates of azimuth, elevation, and range. The spherical data are processed and interpolated to a Cartesian grid before the cross-correlation algorithm is applied. This “pre-processing”, that is applied to each range-dependent lidar backscatter array, includes the calculation and subtraction of the raw background signal, multiplication of the waveform by the range-squared, conversion to decibels, and application of a high-pass median filter. The preprocessed data are then interpolated to a Cartesian grid. In this work, we define a grid with spacing of 10 m in both the east-west and north-south directions. The cross-correlation algorithm can then be applied to any square subset of the Cartesian array. In practice we often start with a 1 km by 1 km square subset containing 100 x 100 data points.

a. The cross-correlation function

The cross-correlation function (CCF) is a measure of the similarity of two arrays, as a function of delay (in time) or lag (in space) applied to one of them. Applied to consecutive frames from a sequence of images, the peak location of the CCF indicates the displacement of the image features within the time interval between the images. The normalized 2D cross-correlation function, $r_{x,y}$, for two series $f_1(x,y)$ and $f_2(x,y)$ is defined as

$$r_{x,y} = \frac{COV_{1,2}}{S_1 S_2}, \tag{1}$$

where $COV_{1,2}$ is the covariance of the overlapped portions of $f_1(x,y)$ and $f_2(x,y)$, S_1 is the standard deviation of $f_1(x,y)$, and S_2 is the standard deviation of $f_2(x,y)$ (Davis and Sampson 2002).

For computational efficiency, the fast Fourier transform (FFT) is widely used instead of the Eqn. (1). Let $f_j(x_m, y_n)$, $j = 1,2$ be discrete signals, N_x the number of data points in the x-direction, N_y the number of points in the y-direction, k_x be the wavenumber corresponding to the x-coordinate, and k_y be the wavenumber corresponding to the y-coordinate. The FFT of image $f_j(x_m, y_n)$, FFT_j can be expressed as

$$FFT_j = \frac{\sum_{m=1}^{N_x} \sum_{n=1}^{N_y} f_j(x_m, y_n) e^{-i2\pi\left(\frac{k_x x_m}{N_x} + \frac{k_y y_n}{N_y}\right)}}{N_x N_y}, \; j = 1,2, \tag{2}$$

and the cross-correlation function $r_{x,y}$ can be expressed as

$$r_{x,y} = \frac{FFT^{-1}(FFT_1 FFT_2^*)}{S_1 S_2}, \tag{3}$$

where FFT_1 is the FFT of $f_1(x,y)$, FFT_2^* is the complex conjugate of FFT_2, and FFT^{-1} represents the inverse fast Fourier transform.

b. Zero-padding

The FFT is designed for periodic signals, but the actual atmospheric lidar images are not periodic. Thus, it is important to circumvent the assumption of periodicity by using "zero-padded" images (Adrian and Westerweel 2011). Each dimension is padded by zeros over a domain that is at least twice the size of the original signal, so three quarters of the 2D interrogation windows are padded by zeros (Bastiaans 2000). The first image block is made by a subset of image at the lower left corner and zeros everywhere in the image block. The second image block is made by the subset of image at the upper right corner and zeros everywhere in the image block. The performance of a cross-correlation algorithm using synthetic backscatter images and synthetic wind velocity fields is increased by using zero-padded images (Hamada 2014).

c. Histogram equalization

Histogram equalization is an image processing technique that enhances image contrast by adjusting the histogram distribution of pixel intensity. Histogram equalization has been used prior to computing the horizontal wind vectors from lidar backscatter images (Schols and Eloranta 1992). Without histogram equalization, the motion of small areas of bright features may dominate the computation of the cross-correlation function. In that case, the cross-correlation may be biased by the motion of such small and bright features. On the other hand, with histogram equalization, other regions in the image are able to influence the cross-correlation function and minimize the bias associated with the motion of the bright features. However, according to the study of Hamada (2014), histogram equalization tends to broaden the cross-correlation function and reduce the performance of the cross-correlation algorithm. Since that study was done based on a relatively strong wind case (wind speed is approximately 10 m s^{-1}), the effects of histogram equalization should be investigated for other cases in the future to determine whether it should be included prior to application of the cross-correlation algorithm for all situations.

d. Tukey window

According to the study of Hamada (2014), the performance of the cross-correlation algorithm decreases if bright features straddle the edges of the interrogation window. This tends to distort the shape of the cross-correlation function, shifts the location of its peak, and leads to an under-estimation of wind velocity vector. Window functions, such as Tukey window, may be applied to taper the backscatter intensity near the image block edges. Let N be the x-dimension of a 1D array. Then, the 1D Tukey window $w(x)$ is defined as

$$w(x) = \begin{cases} \frac{1}{2}(1+\cos[\pi(\frac{2x}{\alpha(N-1)}-1)]) & : 0 \leq x \leq \frac{\alpha(N-1)}{2} \\ 1 & : \frac{\alpha(N-1)}{2} \leq x \leq 1(N-1)(1-\frac{\alpha}{2}) \\ \frac{1}{2}(1+\cos[\pi(\frac{2x}{\alpha(N-1)}-\frac{2}{\alpha}+1)]) & : (N-1)(1-\frac{\alpha}{2}) \leq x \leq (N-1) \end{cases}$$

where α is a constant that determines the width of the cosine lobe of the window (Tukey 1967). It is set to 0.2 for this study. The Tukey window function $w(x)$ can be extended to in 2D via multiplying by $w(y)$ in the y-direction:

$$w(x,y) = w(x)w(y) \tag{4}$$

The Tukey window effectively decreases the intensity of aerosol features straddling the image block edges, thus reducing their undesirable effects.

e. Multi-pass interrogation

The cross-correlation function, for two consecutive lidar backscatter images, gathers contributions from aerosol features that appear in both images. Because aerosol features are advected by the wind, some aerosol features in the first image block may move out of the interrogation window in the time interval between consecutive scans. During the same time, some aerosol features initially outside the first image block may appear in the second image block. In this case, these features do not contribute to the cross-correlation function, and the wind velocity estimation may be biased. For example, if the wind velocity field is non-uniform within an interrogation window, more aerosol features with lower velocity tend to remain within two consecutive image blocks, while those moving faster tend to disappear. In this case, the cross-correlation algorithm is biased and underestimates the wind velocity field in the interrogation window. A multi-pass interrogation Raffel (2007) can minimize such effects. This approach repeats two steps: (i) compute a displacement vector from 2 image blocks by the cross-correlation, then (ii) displace the center of the second block according to this vector. Each vector is an incremental refinement of the solution, and the process loops until the magnitude of the incremental vector falls below 1 pixel – typically, after 2-3 iterations. The sub-pixel location of the peak of the cross-correlation is then estimated by curve fitting. Finally, the solution vector is given by the sum of the incremental estimations and the sub-pixel location. Following this process, the displaced second block contains more features that also appeared in the first image block. The cross-correlation function is therefore better defined, and the accuracy of the motion estimation (wind velocity estimation) increases.

f. Multi-grid interrogation

The cross-correlation algorithm provides one wind velocity vector per interrogation window. The typical size of a large interrogation window, for elastic lidar backscatter images, is about 1000 m $\times$ 1000 m which is larger than the size of most turbulent coherent structures. With a large window size, most microscale structures cannot be resolved although they are important meteorological phenomena. In this case, multi-grid interrogation can be used to increase spatial resolution of the wind velocity vector field. Multi-grid interrogation is similar to multi-pass interrogation except that the dimensions of the image blocks are reduced after each pass (Adrian and Westerweel 2011). In general, the number of features appeared in both image blocks is decreased as the block size is reduced – typically, the reduction factor is 50%. However, displacing the second block increases the similarity of these image blocks, and makes it possible to resolve the wind velocity vector for a relatively small region (less than 500 m $\times$ 500 m). Mayor and Eloranta (2001) applied multi-pass interrogation and multi-grid interrogation but were not able to validate the resulting flow fields.

g. Image deformation

Lidar scans do not represent an instantaneous distribution of aerosol features as in a "snapshot" because of the time required to complete a scan. That is, during a scan some aerosol features are observed before other features, while all features are advected by the wind. The result is a distorted image relative to the ideal snapshot, and the motion estimation is biased. This problem was first discussed by Sasano et al. (1982) who proposed an iterative correction of image deformation. In this process, aerosol features that are observed before and after a reference time within a given scan are translated forward and backward, respectively, according to the mean wind velocity in the entire region of the scan. This process is repeated until the mean velocity is changed by less than 1%. After the image correction, the deformed scan sector approximates a snapshot of the true lidar backscatter distribution at the reference time, here corresponding to the middle of the scan.

h. Quality control

In general, the signal-to-noise ratio (SNR) of elastic backscatter data decays as one over the range squared. In the far range, the noise amplitude may dominate the backscatter from coherent aerosol features. Applying the cross-correlation algorithm to such data can result in areas of spurious, random vectors. In other circumstances, the aerosol features can lead to a peak of the CCF whose location does not represent the actual motion. Such situations are more likely to occur close to the scan edges, or when high wind speeds are involved. They result in isolated spurious vectors, know as outliers. These two distinct sets of erroneous estimates are detected by two different mechanisms inspired from the PIV expertise.

A first step consists in discarding vectors for which the value of the peak of CCF is below a certain threshold. This test is efficient at detecting erroneous vectors resulting from low SNR backscatter data, typically removing patches of vectors in the far range. The second step is handled once the whole vector field has been estimated. It is the *normalized median test*, as described in Adrian and Westerweel (2011). It assumes a local, spatial coherence of the vector field and therefore is able to detect isolated outliers that were missed by the previous test.

For a displacement vector $\mathbf{v}$, these tests can be written as:

$$\left.\begin{array}{ll} \text{if} & r_{v_x,v_y} < \tau_r \text{ (noisy data)} \\ \text{or} & \dfrac{|\mathbf{v}-\mathbf{v_m}|}{\sigma_s+\sigma_\varepsilon} < \tau_m \text{ (isolated outlier)} \end{array}\right\} \Rightarrow \mathbf{v} \text{ discarded,} \tag{5}$$

where $\mathbf{v_m}$ is the median of the 8 vectors $\mathbf{v_i}$ neigboring $\mathbf{v}$, and σ_s is the median of the neighboring residuals $\{|\mathbf{v_i}-\mathbf{v_m}|, i = 1,\ldots,8\}$. In this work, the threshold values are $\tau_r = 0.2$ and $\tau_m = 2$, and $\sigma_\varepsilon = 0.1$. Both of these tests do not depend on the size of the blocks, and can be integrated to a multi-grid interrogation process. They are applied after each step of the multi-grid interrogation. Vectors flagged as spurious are replaced by their value at the previous step of the estimation, if available, and the estimation process stops. As such, the algorithm is adaptive: the estimation proceeds to smaller image blocks (finer motion scales) only when the quality of data is locally good enough to support it.

i. Implementation

A simplified diagram of the operational algorithm is presented Fig. 1. It combines iterations of the distortion correction (Sec. 2.g), the multi-grid (Sec. 2.f) and the multi-pass estimation (Sec. 2.e). For each vector, there can be up to 27 iterations total (3 for each of the distortion correction, multi-grid and multi-pass), with as many evaluations of the CCF. In order to complete the execution of the motion estimation within the time between two scans of the REAL, the core pieces of the method (CCF, histogram equalization, interpolation for the distortion correction) are written in the CUDA language (Mauzey et al. 2012). These functions are executed in a massively parallel fashion on specific graphic processing units that are designed for scientific computation, thus enabling massive real-time execution.

3. Tests using synthetic backscatter images and wind velocity fields

Unlike other wind measurement techniques that sample relatively small volumes of the atmosphere, the cross-correlation algorithm relies upon spatial data over a large area to make a velocity estimate that is assigned to a single point (the location of the center of the interrogation window). The spatial data is the aerosol backscatter field in the interrogation window. If the actual wind velocity is constant throughout the interrogation window, then the spatial distribution of aerosol features that contribute to the cross-correlation function does not matter. However, the wind velocity in the real world is spatially variable. Therefore, it is reasonable to question whether the peak of the cross-correlation function represents the spatial mean of the actual wind field within the interrogation window. This is because the aerosol features may not be evenly distributed across the interrogation window.

In order to study this problem, we developed synthetic velocity fields and synthetic aerosol backscatter images. The synthetic velocity fields enable us to calculate a spatial mean velocity that, although is not continuously defined, is much higher resolution than can be provided by any observing technique. The spatial mean velocity is not currently possible to obtain in the real atmosphere over areas the size of the interrogation window. The synthetic backscatter field enables us to confirm our hypothesis that only a perfectly uniform flow field results in a perfect CCF displacement given a random distribution of aerosol features.

Experiments conducted by Hamada (2014) show that it is possible for the cross-correlation algorithm to provide a velocity vector that does not match the spatial mean over the interrogation window. This problem becomes worse as the inhomogeneity of the velocity field increases, and especially when the spatial distribution of coherent aerosol structures in the backscatter field is also inhomogeneous. The inhomogeneity of the velocity field is the result of coherent flow structures such as areas of convergence, divergence, shear, and vorticity with characteristic length scales of approximately the same size as the interrogation window. These are more likely to occur during periods of weak winds.

In this section of the paper, we present results from experiments conducted with (1) synthetic backscatter fields which are composed of random distributions of aerosol backscatter, and (2) synthetic flow fields where a spatial constant mean wind was added to the turbulent perturbations.

a. Tests for optimization of the cross-correlation algorithm

The performance of the cross-correlation algorithm for wind velocity estimation by elastic lidar was evaluated by using synthetic backscatter images and synthetic wind velocity fields (Hamada 2014). The grid spacing ($\delta x = \delta y = 10$ m) and the time between two consecutive lidar scans ($\delta t = 10$ s) are chosen such that the motion of one unit (10 m) during a time step (10 s) represents a velocity of 1 m s^{-1}.

As a first step, a synthetic backscatter image is created by generating a 2-D array filled with random numbers. The background of the atmospheric aerosol is created by applying a 25 $\times$ 25 pixel boxcar smooth to the random numbers which corresponds to a field of coherent structures with characteristic length of 250 m $\times$ 250 m. Next, small Gaussian features were randomly added in the interrogation window to simulate local sources of aerosol features. Then, a synthetic turbulent velocity perturbation field, as generated by the model of Mann (1994, 1998) is used to diffuse both Gaussian features and background in the interrogation window. Figure 2 shows a synthetic backscatter image and a REAL backscatter image. The REAL backscatter image was extracted from lidar data collected at California State University, Chico, University Farm on October 17, 2013. One pixel of the REAL backscatter image corresponds to the dimensions of 10 m $\times$ 10 m. From Fig. 2, similar spatial gradients and backscatter intensity ranges can be observed in both images although the exact distributions of aerosol features are different.

A synthetic velocity field is created by the sum of a constant flow field and a synthetic turbulent perturbation field. Let $u(x,y)$ and $v(x,y)$ be the east-west and the north-south components of the wind velocity, and $u'(x,y)$, and $v'(x,y)$ be the corresponding components of turbulent perturbations. Then the wind velocity field can be expressed as

$$(u(x,y),v(x,y)) = (C_u + u'(x,y), C_v + v'(x,y)) \tag{6}$$

where C_u and C_v be the corresponding components of constant flow. In this study the following 3 cases are investigated: light wind ($C_u = 1.0$, and $C_v = 0$), moderate wind ($C_u = 5.0$, and $C_v = 0$), and strong wind ($C_u = 10.0$, and $C_v = 0$).

A second image is generated by applying the velocity field and bicubic interpolation to the synthetic backscatter image to displace each pixel of the image to a new location on the Cartesian grid. Then, square subsets of the synthetic backscatter images (image blocks), before and after displacing pixels of the image, are extracted for investigation. Next, the cross-correlation algorithm is applied to these image blocks and the velocity vector is computed. The peak location of the cross-correlation function is estimated by curve fitting (polynomial of degree 2), around the peak (5 $\times$ 5 pixels). The experiment is repeated on 100 different pairs of synthetic backscatter images and the mean and the standard deviation of the velocity vectors are compared with the mean velocity of the given synthetic wind velocity field.

The effects of each option of the cross-correlation algorithm are investigated by 6 different conditions (tests 1, 2, 3, 4, 5, and 6) as shown in Table 1. The image correction, as described by Sasano et al. (1982), is not included for these tests since there is no image distortion for the synthetic lidar backscatter images. The five options of the cross-correlation algorithm are the multi-pass interrogation (MP), the multi-grid interrogation (MG), the zero-padding (ZP), the Tukey window (TW), and the histogram equalization (HE). None of these options are included for test 1, but all five options are included for test 6. The image block size of 25 $\times$ 25 pixels, which corresponds to 250 m $\times$ 250 m regions of REAL backscatter images, is chosen to evaluate the performance of the cross-correlation algorithm in the smallest of block sizes used in the real-time operational version of our algorithm.

b. Results of tests for three cases

Table 2 shows results for the 3 cases (light, moderate, and strong winds). The multi-pass and multi-grid interrogations contribute the most to the performance of the cross-correlation algorithm, the other options bring relatively small improvements. The histogram equalization and the Tukey window tend to slightly underestimate the *u*-component but provide better estimation of the *v*-component, making a correction of the wind-direction estimation. On the other hand, the zero-padding tends to reduce the underestimation of the *u*-component and improve the estimation of the wind speed. Thus, the results suggest that the performance of the cross-correlation algorithm for the relatively small region is optimized by applying all 5 options. In addition, we found that the performance of the cross-correlation algorithm increases as the magnitude of the given velocity vectors decreases. It is likely related to the fact that the two consecutive synthetic backscatter images are more similar for lower velocity treatment.

While the use of synthetic images and flow fields are powerful tools for testing the algorithm, they also have severe limitations and miss relevant physics that occur in the real world. Foremost, our 2D synthetic images and flow fields lack the realism of the 3D nature of aerosol and wind. In the real world, tilted aerosol features may pass through the scan plane resulting in false apparent motions. Also, in the real world, air parcels could move circuitously and not at constant velocity during the time between frames.

4. Comparison with Doppler lidar wind measurements

a. The cross-correlation applied to CHATS

As described by Mayor et al. (2012), a rudimentary cross-correlation algorithm was applied to REAL data collected during the Canopy Horizontal Array Turbulence Study (CHATS, Patton et al. (2011)), from March to June of 2007 near Dixon, California. The REAL was located 1.61 km north of the National Center for Atmospheric Research (NCAR) Integrated Surface Flux Facility (ISFF) 30-m vertical tower. The tower was surrounded by orchard (800 m $\times$ 800 m) of walnut trees approximately 10-m tall. 5 Campbell Scientific CSAT3 3D sonic anemometers were located on the tower at 12.5, 14.0, 18.0, 23.0 and 29.0 m above ground level (AGL) to measure the wind velocity. The REAL scanned the atmosphere horizontally (the plan position indicator, PPI) over the orchard, and the rudimentary cross-correlation algorithm was applied to estimate the wind velocity in a 1000 m $\times$ 1000 m region surrounding the tower.

The REAL dataset from CHATS was groundbreaking but it had some deficiencies. In particular, the ISFF tower and nearby trees caused hard-target reflections, creating non-stationary bright pixels and large shadows in the aerosol backscatter data that prevented optimal retrieval of wind fields by the cross-correlations. Moreover, the REAL platform settled into the soil during the course of the CHATS experiment and precise measurements of the pitch and roll of the instrument were not available. This resulted in uncertainty of the altitude of the REAL beam at the location of the ISS vertical tower. Given the strong speed shear with increasing altitude in the roughness sublayer just above the top of the canopy, Mayor et al. (2012) choose not to calculate and compare mean wind velocity data and instead focused on the instantaneous wind vectors resulting from the cross-correlation algorithm.

In order to move forward, a new field experiment was conducted in Chico, California, from May of 2013 through January of 2014. Chico is 130 km north of Dixon and has less variable relative humidity than Dixon due to its distance from the Sacramento-San Joaquin River Delta. However, nearby agriculture activities and convection offer good conditions for testing. In the Chico Experiment, a Streamline Doppler lidar (from Halo Photonics) was employed as the reference system in order to avoid hard target reflections, it measured winds 30 - 170 m AGL. The wind measurement using the DL was previously validated against cup anemometers (Smith et al. 2006). The REAL was on firm ground and pitch and roll of the platform was recorded to ensure precise knowledge of the altitude of the laser beam as a function of range. Both the REAL and the DL data acquisition systems were time synchronized to GPS time. Since a single DL cannot retrieve a 2D 2-component wind velocity field, the following configurations were investigated.

b. Temporal validation

The DL was located 1523 m from the REAL in the direction of 15° azimuth. In order to test the technique at the height of typical wind turbines and above the reach of typical meteorological towers, the DL was operated in vertical profile mode (VAD scan of radius 107 m at 100 m AGL and an angle 43° from the horizontal) to provide horizontal components of the wind velocity vector every 17 s. The REAL system scanned the atmosphere between -15° and 45° azimuth, at 4° elevation, in about 15 s. Then, the optimized cross-correlation algorithm with all options (MP, MG, HE, ZP, and TW), was applied to estimate the wind velocity in an image block of the dimensions 250 m × 250 m centered directly over the DL at the altitude of 100 m AGL. The image correction, as discussed by Sasano et al. (1982), was applied to all REAL backscatter images before the wind velocity estimation. Figures 3 and 4 show the experimental setup at the California State University, Chico, farm. Figure 5 shows the data density for REAL system (+) and the DL (•) within an image block for the cross-correlation, 250 m × 250 m, at the altitude of 100 m AGL. Both the REAL system and the DL estimated the wind velocity vectors every 17 s, and time series of the wind velocity vectors were compared.

The quality of aerosol backscatter data depends upon the performances of the instrument and the state of the atmosphere. In the following, three cases featuring different wind conditions are presented: low, moderate and strong wind speeds. Then, a statistical analysis of 15 days that occurred in September and October of 2013 is considered. These 15 days present the highest amount of valid data at the DL location during daytime, while covering a broad range of wind velocities (0–16 m s^{-1}) and constant to variable wind directions. Therefore, these days constitute the best set to analyze the performance of the algorithm while minimizing the effects of the instrument and atmosphere. They were selected by analyzing the "image SNR" as detailed in Dérian et al. (2015).

1) Light wind case

Figure 6 shows time series of wind speeds and directions, as estimated by the DL (blue), and by the optimized cross-correlation algorithm (green) from REAL backscatter images for a 12-hour period starting from 23 October 2013 15:00 UTC. This is an example of a light wind case where the wind speed is between 0 m s^{-1} and 2 m s^{-1} and the wind direction is variable. The results show that the time series of both methods are very similar except a 2-hour period between 15:00 and 17:00 UTC, where no coherent aerosol features were present. Correlation coefficients R^2 for the 10-minute averaged wind speed and direction between the optimized cross-correlation and the DL are, 0.829, and 0.658, respectively.

2) Moderate wind case

Figure 7 shows time series of wind speeds and directions, as estimated by the DL (blue), and by the optimized cross-correlation algorithm (green) from REAL backscatter images for a 12-hour period starting from 17 September 2013 15:00 UTC. Points represent the individual estimates and the line a 10-minute rolling average. This is an example of a moderate wind case where the wind speed varies between 0 m s^{-1} and 8 m s^{-1} and the wind direction is approximately constant for the first half of the period, but varies after 20:00 UTC. Time series of both methods are remarkably similar for both wind speed and direction. Correlation coefficients R^2 for the 10-minute averaged wind speed and direction between the optimized cross-correlation and the DL are, 0.973, and 0.938, respectively.

3) Strong wind case

Figure 8 shows time series of wind speeds and directions, as estimated by the DL (blue), and by the optimized cross-correlation algorithm (green) from REAL backscatter images for a 12-hour period starting from 9 October 2013 at 15:00 UTC. Points represent the individual estimates and the line a 10-minute rolling average. This is an example of a strong wind case where the wind speed is about 10 m s^{-1} (up to 14 m s^{-1}) and the wind direction is approximately constant (from the northwest direction). As in the moderate wind case the time series of both methods are strikingly similar for both wind speed and direction. Correlation coefficients R^2 for the 10-minute averaged wind speed and direction between the optimized cross-correlation and the DL are, 0.929, and 0.968, respectively.

4) Statistical analysis of temporal validation

Statistical comparisons between optimized cross-correlation and the DL are summarized in Tables 3 and 4 for all three cases (weak, moderate and strong wind). Figure 9 presents scatter plots for the 10-minute means collected over 15 days (891 intervals), and corresponding statistical results are available in Tables 3 and 4. The scatter plots show an excellent agreement between the cross-correlation motion estimates and the DL measurements. This is confirmed by the R^2 coefficients, with values of 0.993 and 0.995 for components u and v, respectively.

The time-series of Figs. 6, 7 and 8 reveals that the wind velocities obtained from the cross-correlation have a lesser variability than the Doppler measurements. Figure 10 shows scatter plots of the turbulent kinetic energy (TKE) measured by the Doppler and the cross-correlations over the 891 10-minute intervals . Three sets of results are presented for the cross-correlations, corresponding to 3 levels of the multi-grid estimation: 1000 m $\times$ 1000 m, 500 m $\times$ 500 m and 250 m $\times$ 250 m. In all 3 sets, the cross-correlation method underestimated the TKE. However, as the block size is reduced, more TKE is recovered: from $\approx$25% with the largest blocks to $\approx$39% with 250 m $\times$ 250 m blocks. These results highlight that smaller block sizes are able to capture smaller perturbations. As stated in Mayor et al. (2012), estimating directly from small block sizes leads to noisier results. With the addition of multi-pass, multi-grid and quality control, the proposed optimized algorithm is now able to increase the resolution of the motion field.

c. Spatial validation

For this phase of the experiment, the DL was located on the roof of the REAL system and operated in fixed-beam mode pointing at 45° azimuth and 2° elevation to estimate the radial component of the wind velocity field at the center of the scan sector swept by the REAL. The corresponding radial component of the wind velocity was retrieved from the horizontal components of wind velocity vector estimated by optimized cross-correlation algorithm applied to REAL backscatter images.

The radial components of the wind velocity vectors at 45° azimuth and 2° elevation were retrieved by the optimized cross-correlation algorithm with all options (MP, MG, HE, ZP, and TW) applied to image blocks (250 m $\times$ 250 m) in the range between 0.5 km and 3 km from the REAL system. The REAL system scanned the atmosphere every 17 s (between 15° and 75° azimuth at 2 elevation). Then the radial component of the wind vectors as a function of time and range were compared. This experiment was conducted in December 2013 and January 2014.

Figure 11 shows the radial component of the wind velocity as measured by the DL and estimated by the optimized cross-correlation algorithm, for an 8-hour period starting 8 January 2014 at 17:00 UTC. It suggests strong correlation of the two radial velocity fields.

Statistics on the 10-minute mean radial velocities, computed at different ranges, are presented Fig. 12. These results where computed over 8-hour periods (from 17:00 to 01:00 UTC) of 8 days selected in December 2013 and January 2014. It shows that the R^2 coefficient (panel d) remains above 0.97 until 1.2 km range, then decreases with the range due to the decaying SNR for both instruments. The scatter plot of radial velocities (panel a) indicates that the cross-correlations gradually overestimate the radial velocities as the range increases. This is confirmed by the histogram of velocity differences (panel b), biased towards negative values, as well as the slopes of linear regressions (panel c). A similar trend was found for the same dataset using a different motion estimation method (Dérian et al. 2015). This likely indicates a slight misalignment of both instrument beams. A mismatch in the elevation angle would result in a difference in altitude of the beams that increases with the range, thus explaining the lower velocities measured by the DL.

d. Wind velocity fields

The 2-component wind velocity fields can be retrieved from the REAL backscatter images up to several km via application of the optimized cross-correlation algorithm. Figure 13 shows an example of a strong wind case where the wind velocity is approximately uniform up to about 4 km from the REAL system. Figure 14 shows an example of a vortex observed from the light wind case (23 October, 2013). Since the radius of the vortex is about 200 m, we cannot observe such a structure without the use of the optimized cross-correlation algorithm.

5. Conclusions

This paper describes the results of a research program that utilized two very different approaches to characterizing and improving the performance of the cross-correlation algorithm as applied to elastic lidar data for remote wind estimation. The first approach, described in detail in Hamada (2014), involved the use of synthetic aerosol backscatter fields and synthetic turbulent velocity fields to conduct highly controlled numerical experiments. The synthetic test results are significant because they confirm that the peak of the cross-correlation function estimates the mean of the actual velocity field (when the flow is uniform). No other physical method to our knowledge exists to obtain a vector at 10 m grid spacing over a 250 x 250 m area in order to confirm the hypothesis that the peak of the CCF matches the mean of the actual flow field. The synthetic test results were also informative in that they verify loss of precision as the flow field as the flow field becomes less uniform. In the future, large eddy simulations could be used refine the general theory supporting this method of wind estimation.

By utilizing synthetic images and velocity fields, Hamada (2014) was able to determine the required steps and evaluate the significance of their impact on the resulting motion vectors. An operational real-time version of the optimized cross-correlation algorithm is now available for use with the REAL.

The second approach involved a field experiment. When sufficient small-scale aerosol structures are present, the 10-min mean wind estimates from the optimized cross-correlation algorithm (for a single point within the scan area) match that obtained from a calibrated vertically profiling Doppler lidar, with correlation coefficients R^2 above 0.99 for the two horizontal components. By comparing the variance of the non-averaged velocity components, we determined that the cross-correlation algorithm only results in 39% of the TKE measured by the Doppler lidar. It is important to keep in mind that the Doppler lidar variance is also an underestimate of the true TKE due to its pulse volume and scan strategy.

The above suggests that the approach of using a horizontally scanning aerosol lidar, like the REAL, and motion estimation algorithms to observe the mean wind may be of value in situations where it is difficult or impossible to deploy a profiling Doppler lidar. Moreover, a horizontally scanning lidar can provide spatial wind velocity information. This may also be of interest in situations where the air flow may be horizontally inhomogeneous. The flow fields produced by the technique contain two components, which are required in order to determine both wind speed and direction.

Acknowledgments. This material is based upon work supported by the National Science Foundation's Physical and Dynamic Meteorology Program under Grant No. AGS 1228464.

References

Adrian, R. J., and J. Westerweel, 2011: *Particle Image Velocimetry*. Cambridge University Press.

Antoine, E., C. Buchanan, K. Fezzaa, W.-K. Lee, M. N. Rylander, and P. Vlachos, 2013: Flow measurements in a blood-perfused collagen vessel using x-ray micro-particle image velocimetry. *PLOS ONE*, **8 (11)**, e81 198.

Avants, B. B., C. L. Epstein, M. Grossman, and J. C. Gee, 2008: Symmetric diffeomorphic image registration with cross-correlation: evaluating automated labeling of elderly and neurodegenerative brain. *Med. Image Anal.*, **12 (1)**, 26–41.

Bastiaans, R. J., 2000: *Cross-correlation PIV: Theory, Implementation and Accuracy*. Eindhoven University of Technology, Faculty of Mechanical Engineering.

Cheng, W., Y. Murai, T. Sasaki, and F. Yamamoto, 2005: Bubble velocity measurement with a recursive cross correlation PIV technique. *Flow Meas. Instrum.*, **16 (1)**, 35–46.

Corpetti, T., D. Heitz, G. Arroyo, E. Memin, and A. Santa-Cruz, 2006: Fluid experimental flow estimation based on an optical-flow scheme. *Exp. Fluids*, **40 (1)**, 80–97.

Davis, J. C., and R. J. Sampson, 2002: *Statistics and Data Analysis in Geology*. Wiley.

Dérian, P., C. F. Mauzey, and S. D. Mayor, 2015: Wavelet-based optical flow for two-component wind field estimation from single aerosol lidar data. *Submitted to J. Atmos. Ocean. Technol.*

Eloranta, E. W., J. M. King, and J. A. Weinman, 1975: The determination of wind speeds in the boundary layer by monostatic lidar. *J. Appl. Meteor.*, **14**, 1485–1489.

Emery, W. J., D. Baldwin, and D. Matthews, 2003: Maximum cross correlation automatic satellite image navigation and attitude corrections for open-ocean image navigation. *IEEE T. Geosci. Remote Sens.*, **41 (1)**, 33–42.

Hamada, M., 2014: Evaluation of the performance of a cross-correlation algorithm for wind velocity estimation using synthetic backscatter lidar images and velocity fields. diploma thesis, California State University, Chico, 400 West First Street, Chico CA 95929.

Kolev, I., O. Parvanov, and B. Kaprielov, 1988: Lidar determination of winds by aerosol inhomogeneities: motion velocity in the planetary boundary layer. *Appl. Optics*, **27**, 2524–2531.

Leese, J. A., C. S. Novak, and B. B. Clark, 1971: An automated technique for obtaining cloud motion from geosynchronous satellite data using cross correlation. *J. Appl. Meteorol.*, **10 (1)**, 118–132.

Mann, J., 1994: The spatial structure of neutral atmospheric surface-layer turbulence. *J. Fluid Mech.*, **273**, 141–168.

Mann, J., 1998: Wind field simulation. *Prob. Engng. Mech.*, **13**, 269–282.

Mauzey, C. F., J. P. Lowe, and S. D. Mayor, 2012: Real-time wind velocity estimation from aerosol lidar data using graphics hardware. *GPU Technology Conference*, San Diego, CA, poster AV10.

Mayor, S. D., and E. W. Eloranta, 2001: Two-dimensional vector wind fields from volume imaging lidar data. *J. Appl. Meteor.*, **40**, 1331–1346.

Mayor, S. D., J. P. Lowe, and C. F. Mauzey, 2012: Two-component horizontal aerosol motion vectors in the atmospheric surface layer from a cross-correlation algorithm applied to scanning elastic backscatter lidar data. *J. Atmos. Ocean. Technol.*, **29**, 1585–1602.

Mayor, S. D., and S. M. Spuler, 2004: Raman-shifted Eye-safe Aerosol Lidar. *Appl. Optics*, **43**, 3915–3924.

Mayor, S. D., S. M. Spuler, and B. M. Morley, 2005: Scanning eye-safe depolarization lidar at 1.54 microns and potential usefulness in bioaerosol plume detection. *Lidar Remote Sensing for Environmental Monitoring VI*, SPIE, Paper 5887–23.

Mayor, S. D., S. M. Spuler, B. M. Morley, and E. Loew, 2007: Polarization lidar at 1.54-microns and observations of plumes from aerosol generators. *Opt. Eng.*, **46**, DOI: 10.1117/12.781 902.

Murray, J. C., H. R. Erwin, and S. Wermter, 2009: Robotic sound-source localisation architecture using cross-correlation and recurrent neural networks. *Neural Networks*, **22 (2)**, 173–189.

Patton, E. G., and Coauthors, 2011: The Canopy Horizontal Array Turbulence Study (CHATS). *Bull. Amer. Meteor. Soc.*, **92**, 593–611.

Raffel, M., 2007: *Particle Image Velocimetry: A Practical Guide*. Springer.

Rinehart, R. E., and E. T. Garvey, 1978: Three-dimensional storm motion detection by conventional weather radar. *Nature*, **273**, 287–289.

Sasano, Y., H. Hirohara, T. Yamasaki, H. Shimizu, N. Takeuchi, and T. Kawamura, 1982: Horizontal wind vector determination from the displacement of aerosol distribution patterns observed by a scanning lidar. *J. Appl. Meteor.*, **21**, 1516–1523.

Schols, J. L., and E. W. Eloranta, 1992: The calculation of area-averaged vertical profiles of the horizontal wind velocity from volume imaging lidar data. *J. Geophys. Res*, **97**, 18 395–18 407.

Schubert, A., A. Faes, A. Kääb, and E. Meier, 2013: Glacier surface velocity estimation using repeat TerraSAR-X images: Wavelet vs. correlation-based image matching. *Int. Soc. Photogramme.*, **82**, 49–62.

Shimizu, H., Y. Sasano, Y. Yasuoka, H. Ueda, N. Takeuchi, and M. Okuda, 1981: The remote measurement of wind direction and velocity by a laser radar using the spatial correlation technique. *Oyobutsuri*, **50**, 616–620.

Smith, D. A., M. Harris, A. S. Coffey, T. Mikkelsen, H. E. Jørgensen, J. Mann, and R. Danielian, 2006: Wind lidar evaluation at the Danish wind test site in Høvsøre. *Wind Energy*, **9 (1-2)**, 87–93.

Stawiarski, C., K. Träumner, C. Knigge, and R. Calhoun, 2013: Scopes and challenges of dual-Doppler lidar wind measurementsan error analysis. *J. Atmos. Ocean. Technol.*, **30 (9)**, 2044–2062.

Tukey, J. W., 1967: *An introduction to the calculations of numerical spectrum analysis*, 25–46. John Wiley and Sons.

LIST OF TABLES

TABLE 1. The tests of the cross-correlation algorithm using synthetic backscatter images and the velocity fields. The five options of the cross-correlation algorithm are, the multi-pass interrogation (MP), the multi-grid interrogation (MG), the zero-padding (ZP), the Tukey window (TW), and the histogram equalization (HE). ✓ and × represent that these options are turned on or off, respectively.

Options	*MP*	*MG*	*HE*	*ZP*	*TW*
Test 1	×	×	×	×	×
Test 2	✓	×	×	×	×
Test 3	✓	✓	×	×	×
Test 4	✓	✓	✓	×	×
Test 5	✓	✓	✓	✓	×
Test 6	✓	✓	✓	✓	✓

TABLE 2. The results of the tests of the cross-correlation algorithms using synthetic backscatter images for light (top), moderate (middle), and strong (bottom) wind cases. The 2D synthetic velocity field and the test results are expressed in (pixels / frames). The first and the second rows show the mean velocity and the standard deviation (SD), respectively, obtained from 100 estimations.

	Velocity field	Test 1	Test 2	Test 3	Test 4	Test 5	Test 6
Mean	(1.027, 0.002)	(0.509, 0.008)	(0.563, 0.008)	(1.018, -0.001)	(0.988, 0.001)	(1.006, 0.001)	(1.008, 0.002)
SD		(0.282, 0.063)	(0.345, 0.060)	(0.192, 0.011)	(0.187, 0.007)	(0.004, 0.002)	(0.014, 0.011)
Mean	(5.811, 0.088)	(3.538, -0.005)	(4.282, -0.154)	(5.676, -0.036)	(5.648, 0.156)	(5.718, 0.154)	(5.608, 0.142)
SD		(1.891, 1.155)	(1.901, 2.202)	(0.394, 0.493)	(0.383, 0.165)	(0.309, 0.153)	(0.452, 0.191)
Mean	(11.79, 0.194)	(5.305, -0.134)	(6.575, 0.748)	(11.70, -0.672)	(11.64, 0.612)	(11.68, 0.766)	(11.32, 0.586)
SD		(6.654, 4.579)	(8.139, 17.39)	(0.798, 1.173)	(0.795, 0.658)	(0.752, 0.810)	(0.498, 0.749)

TABLE 3. Standard deviation of differences, linear regression variables (slope, offset), correlation coefficient R^2, number of points and recovery percentage w.r.t. DL reference for the 10-minute averaged wind component u (west-east), for the 3 specific cases and the 15 days considered for the temporal validation.

case	std dev (m s^{-1})	slope	offset (m s^{-1})	R^2	# points	% recovery
light	0.15	0.984	0.079	0.950	64	88.9
moderate	0.34	0.937	-0.06	0.971	72	100
strong	0.48	0.947	0.16	0.961	72	100
15 days	0.35	0.974	-0.05	0.993	891	99.0

TABLE 4. Standard deviation of differences, linear regression variables (slope, offset), correlation coefficient R^2, number of points and recovery percentage w.r.t. DL reference for the 10-min averaged wind component v (south-north), for the 3 specific cases and the 15 days considered for the temporal validation.

case	std dev (m s^{-1})	slope	offset (m s^{-1})	R^2	# points	% recovery
light	0.33	0.504	0.020	0.458	64	88.9
moderate	0.28	0.984	0.01	0.987	72	100
strong	0.44	0.885	-0.76	0.879	72	100
15 days	0.37	0.991	0.06	0.995	891	99.0

LIST OF FIGURES

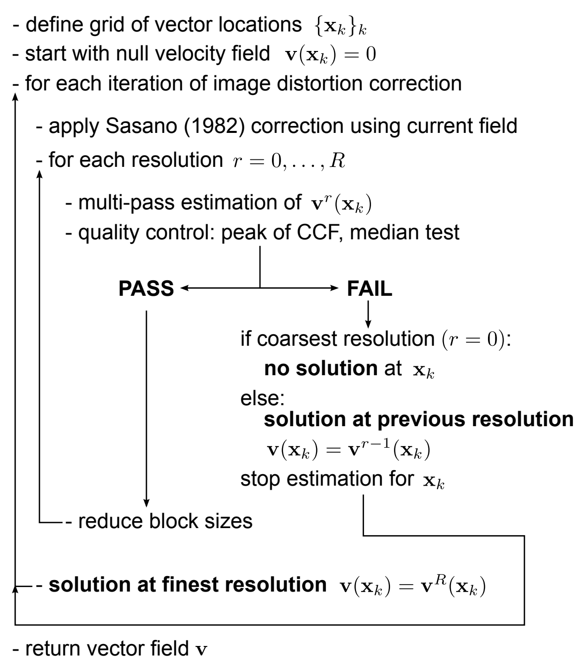

FIG. 1. Simplified diagram of the cross-correlation algorithm.

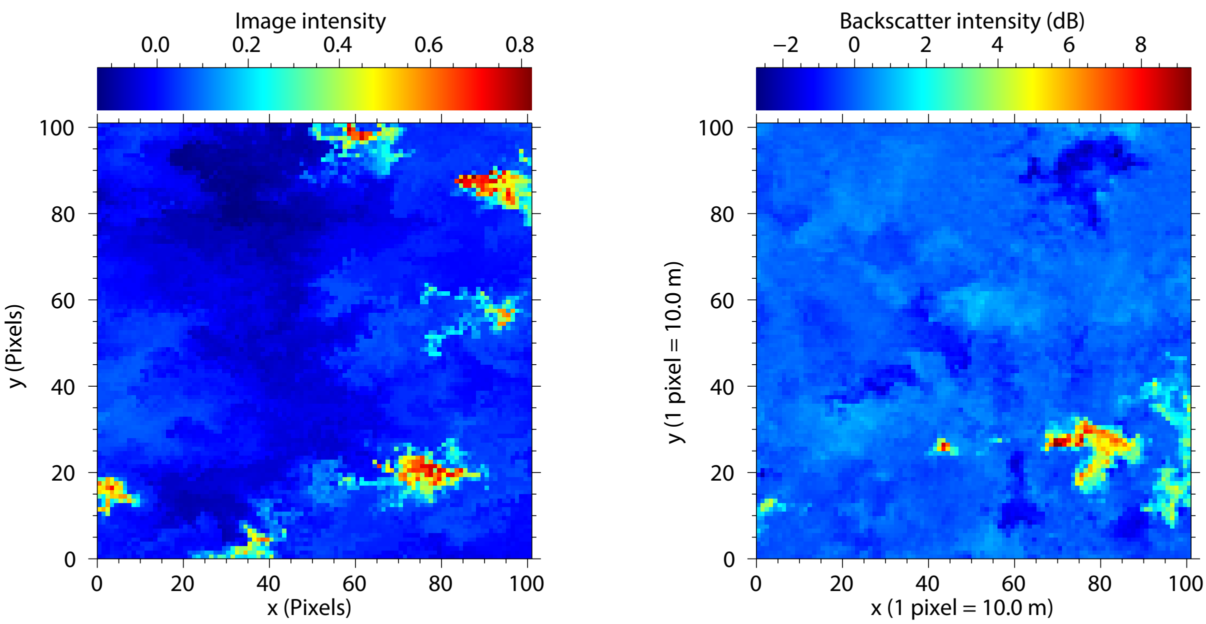

FIG. 2. Comparison of a synthetic backscatter image (left) and a REAL backscatter image (right) The REAL backscatter image was collected at the California State University, Chico, University Farm, on October 17, 2013.

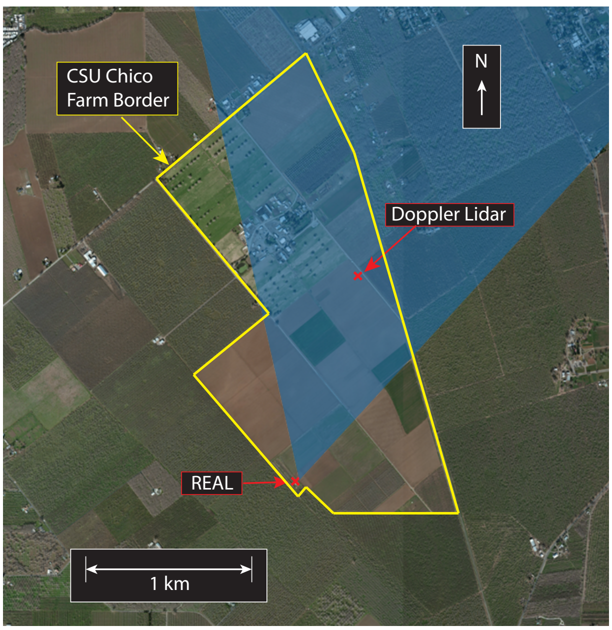

FIG. 3. A map showing the experimental setup at the California State University Chico, University Farm in 2013. The yellow lines represent the University Farm border. The two red × represent the locations of the REAL system and the Doppler lidar (DL), respectively. The blue region represents the PPI scans collected by the REAL system for the experiment.

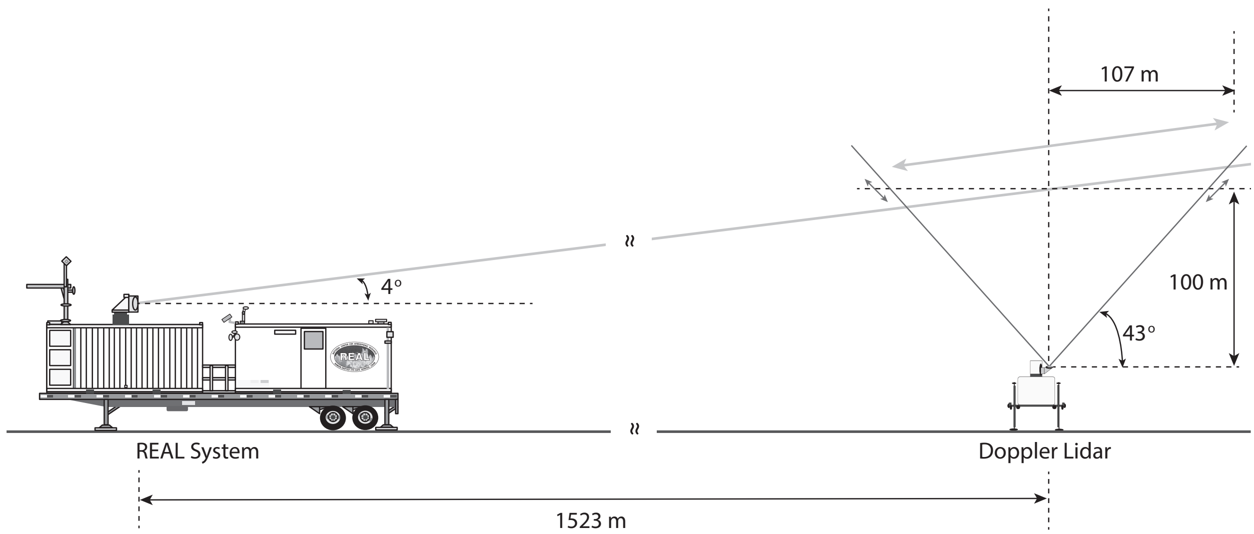

669 FIG. 4. Vertical cross-section diagram for the 2013 Chico field experiment. The REAL scans the atmosphere
670 at 4° elevation. The DL is located 1523 m from the REAL and operated in vertical profile mode. With an
671 elevation angle of 43°, the DL samples at 100 m AGL were 107 m from the center location.

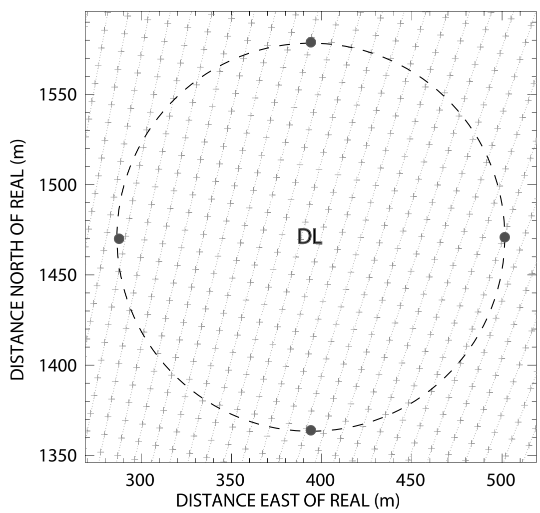

FIG. 5. Diagram of lidar data density in a 250 m × 250 m area at 100 m above the DL location. REAL aerosol backscatter (+) and DL radial velocity measurement (•).

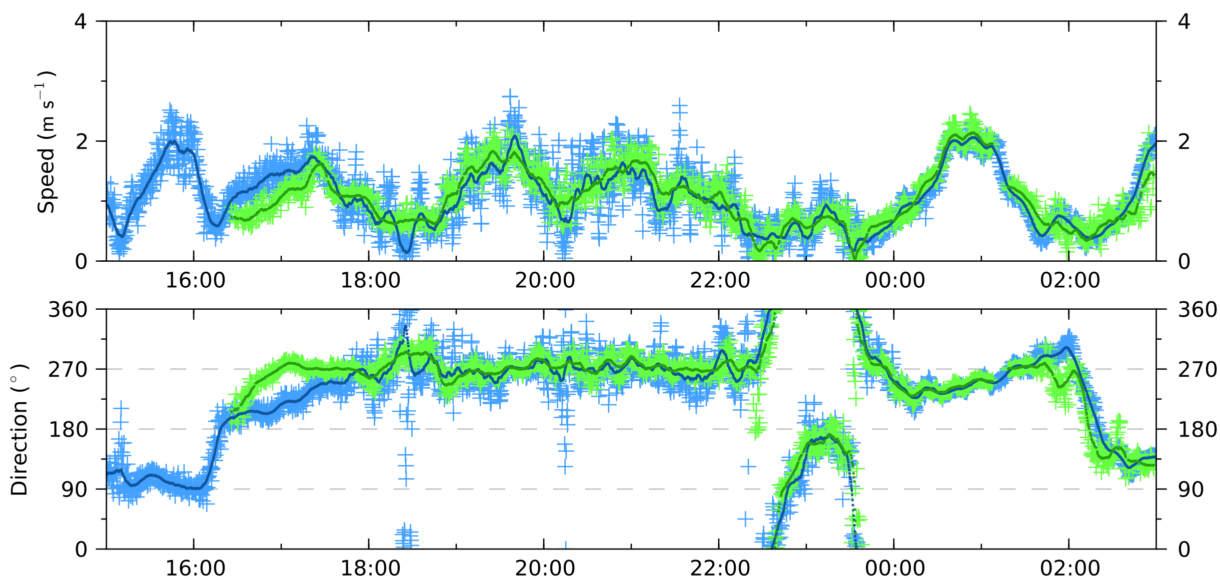

674 FIG. 6. Time series of wind speed and direction, as estimated by the DL (blue), and by the optimized cross-correlation algorithm (green) from REAL backscatter images for a light wind case starting at 15:00 UTC on 23 October 2013. Each (+) represents individual estimation or measurement, separated by approximately 17 s. Solid lines represent 10-minute rolling averages.

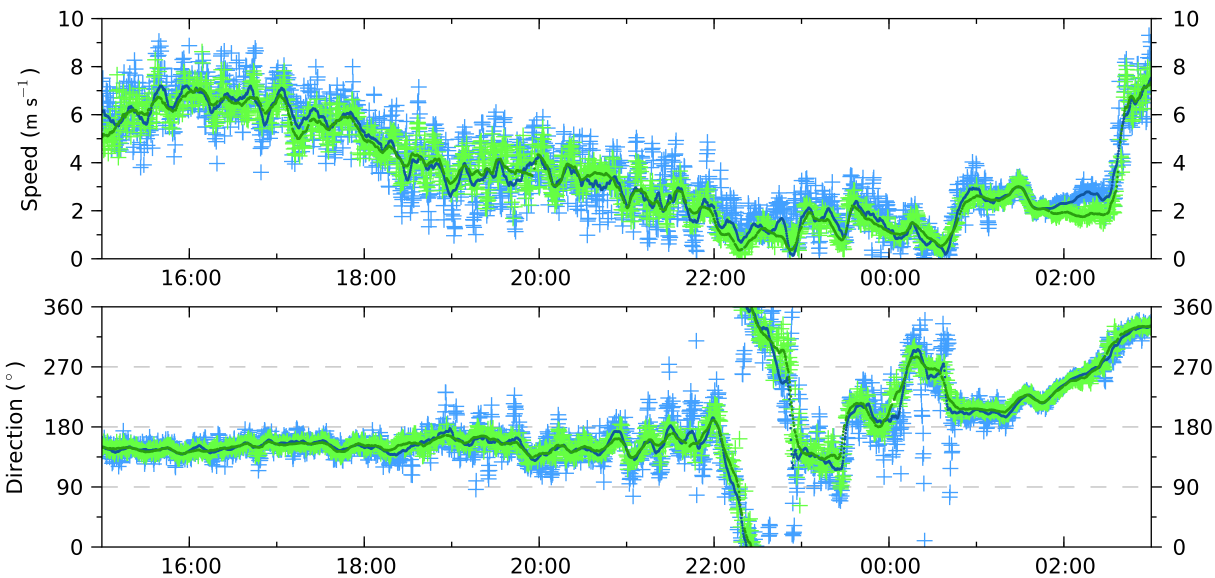

FIG. 7. Time series of wind speed and direction, as estimated by the DL (blue), and by the optimized cross-correlation algorithm (green) from REAL backscatter images for a moderate wind case starting at 15:00 UTC on 17 September 2013. Each (+) represents individual estimation or measurement, separated by approximately 17 s. Solid lines represent 10-minute rolling averages.

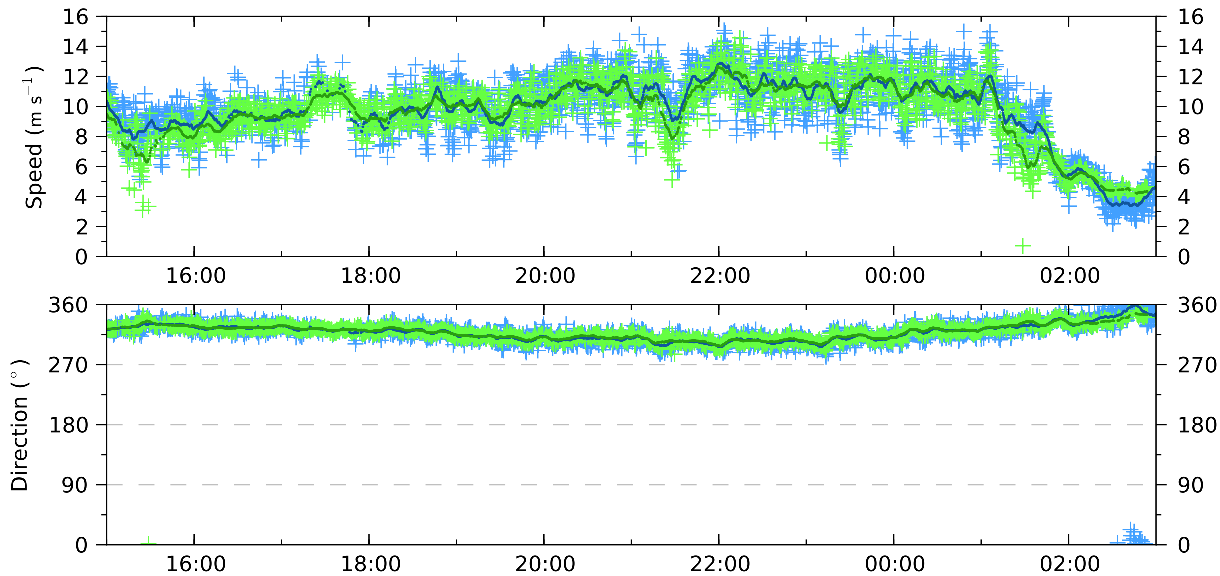

682 FIG. 8. Time series of wind speed and direction, as estimated by the DL (blue), and by the optimized cross-correlation algorithm (green) from REAL backscatter images for a strong wind case starting at 15:00 UTC on 9 October 2013. Each (+) represents individual estimation or measurement, separated by approximately 17 s. Solid lines represent 10-minute rolling averages.

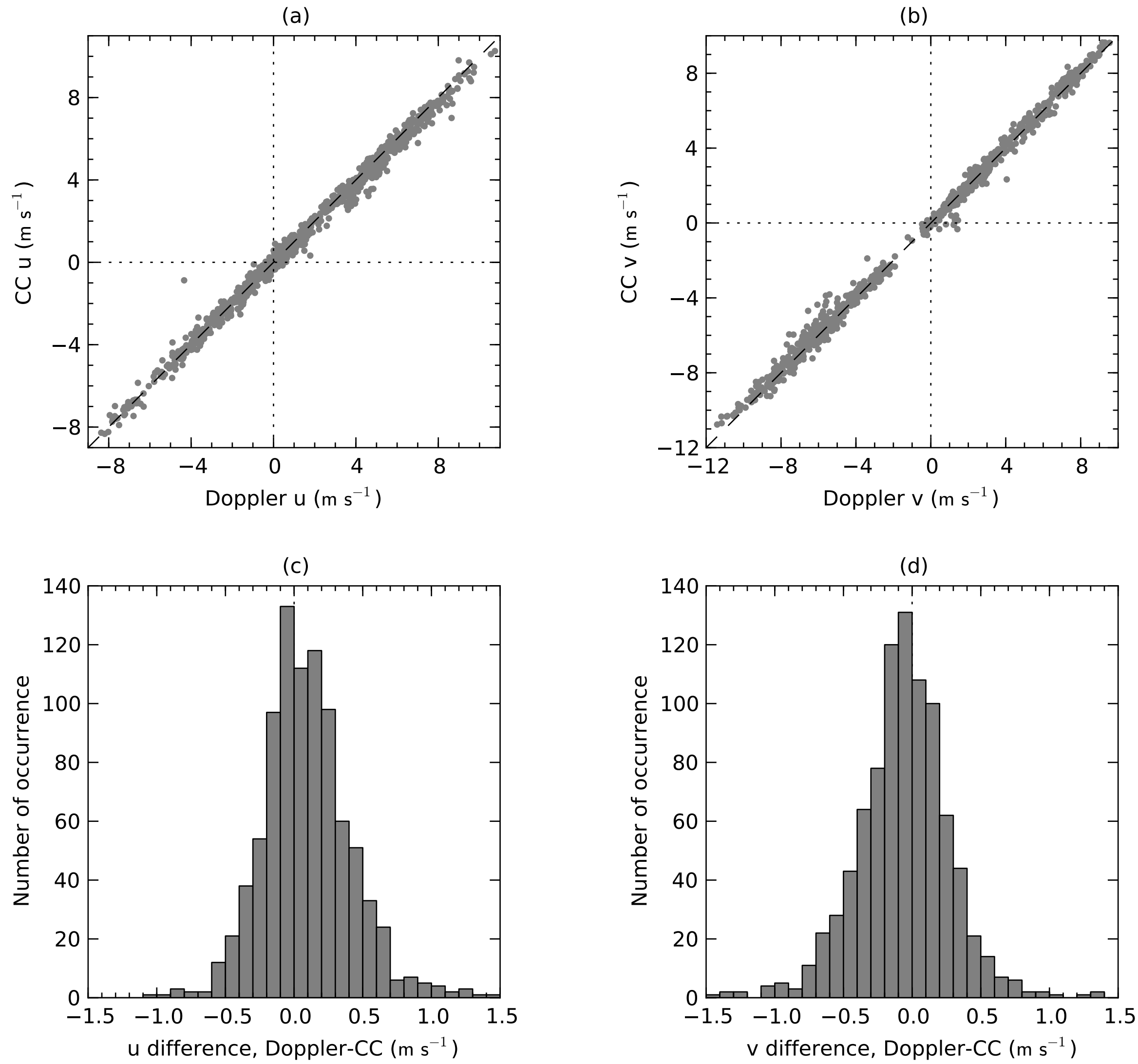

FIG. 9. Scatter plots (Top) of 10-minutes averaged *u*- and *v*- components of the wind velocity estimated by the optimized cross-correlation algorithm (vertical axis) versus that estimated by the DL at 100 m AGL (horizontal axis), for 15 days, during daytime (891 intervals). The histogram distribution of differences for the same dataset are shown in the bottom panels.

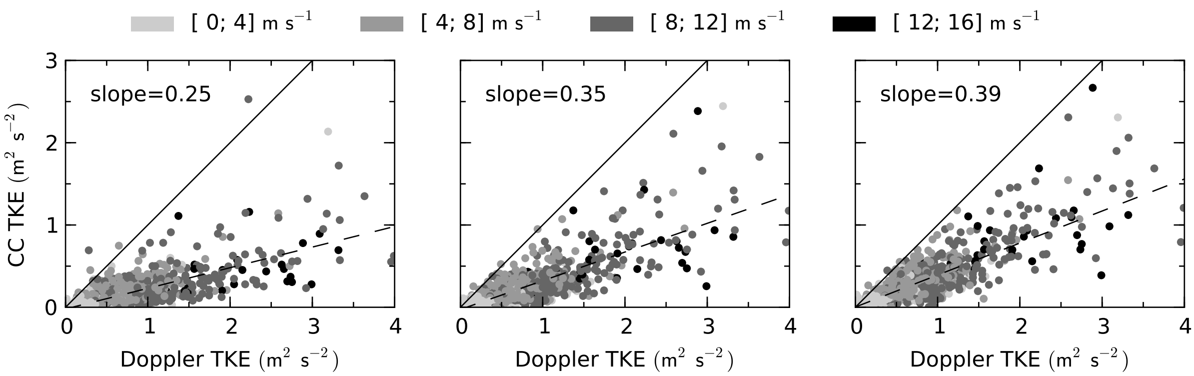

FIG. 10. TKE of the cross-correlation wind estimates (vertical axis) versus Doppler wind measurements (horizontal axis) computed from 891 10-minute intervals. The gray shading indicates the mean wind speed measured over the interval. The 3 sets correspond to block sizes of 1000 m × 1000 m (left), 500 m × 500 m (middle) and 250 m × 250 m (right).

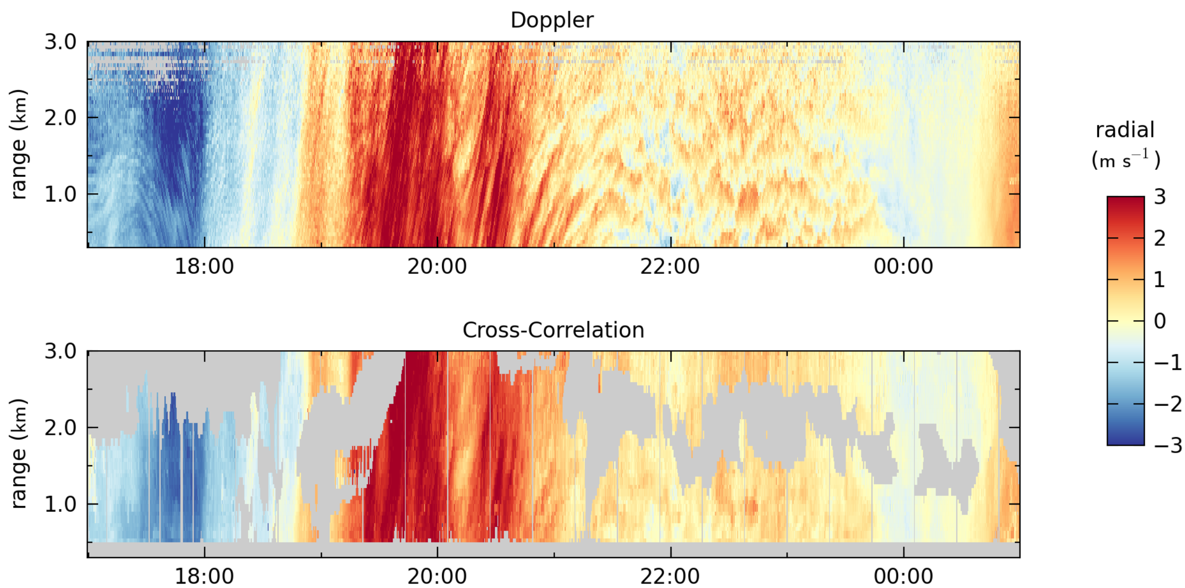

FIG. 11. Range-versus-time images of radial velocity from the DL (top) and optimized cross-correlation algorithm applied to the REAL backscatter images (bottom), for a 8-hour period starting from 8 January 2014 at 17:00 UTC. Grey shading indicates data discarded by quality control, likely associated with the absence of aerosol structures.

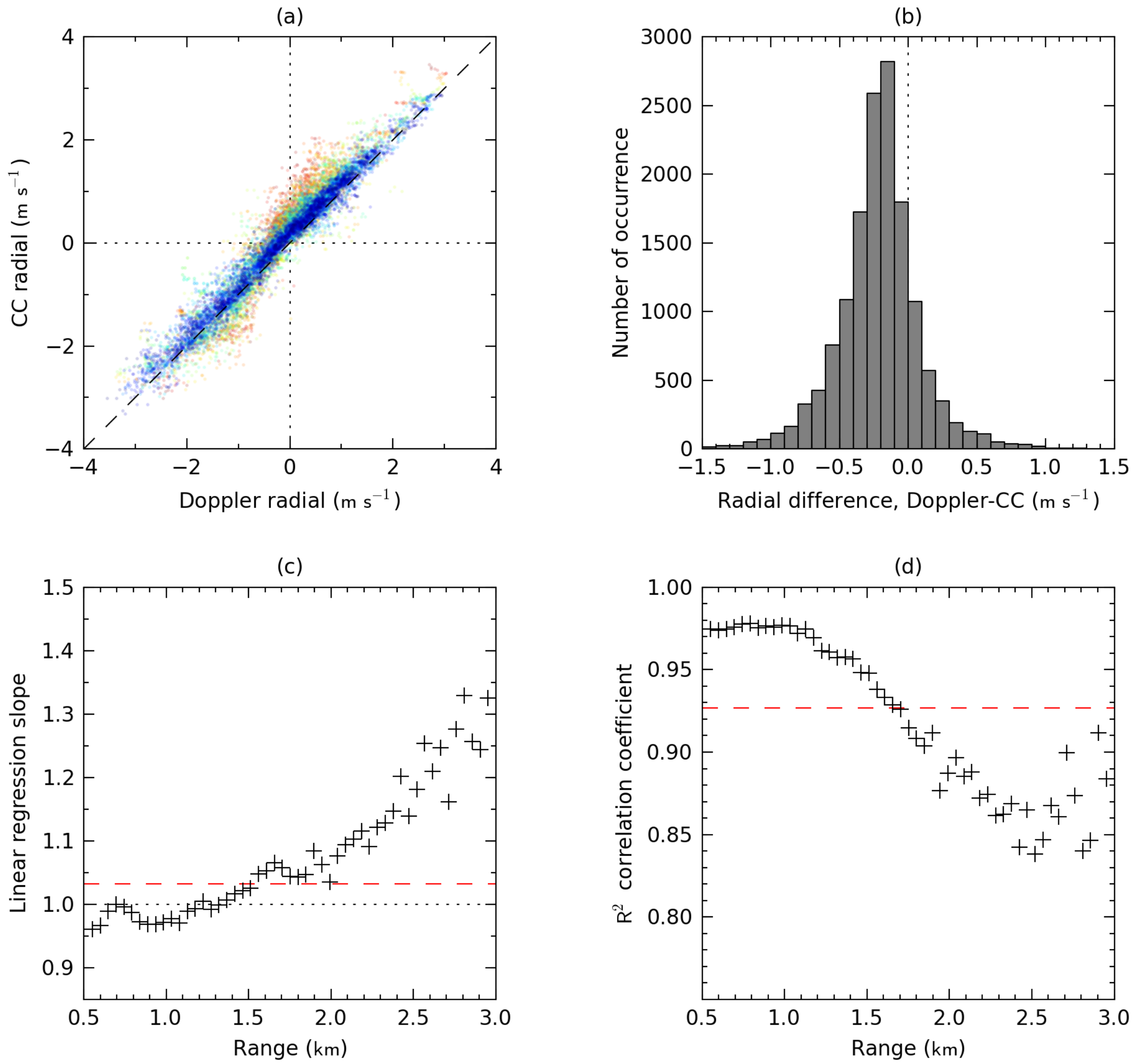

FIG. 12. Panel (a), scatter plot of 10-minute averaged radial component of the wind velocity vector, as estimated by the optimized cross-correlation algorithm (vertical axis) versus that estimated by the DL (horizontal axis). Color indicates the range, from blue (0.5 km) to red (3 km). Panel (b), histogram of difference of radial component of the wind velocity vector. Panel (c), slope of linear regression (vertical axis) as a function of range (horizontal axis). Dashed red line indicates overall slope. Panel (d), R^2 coefficient (vertical axis) as a function of range (horizontal axis). Dashed red line indicates overall R^2 value.

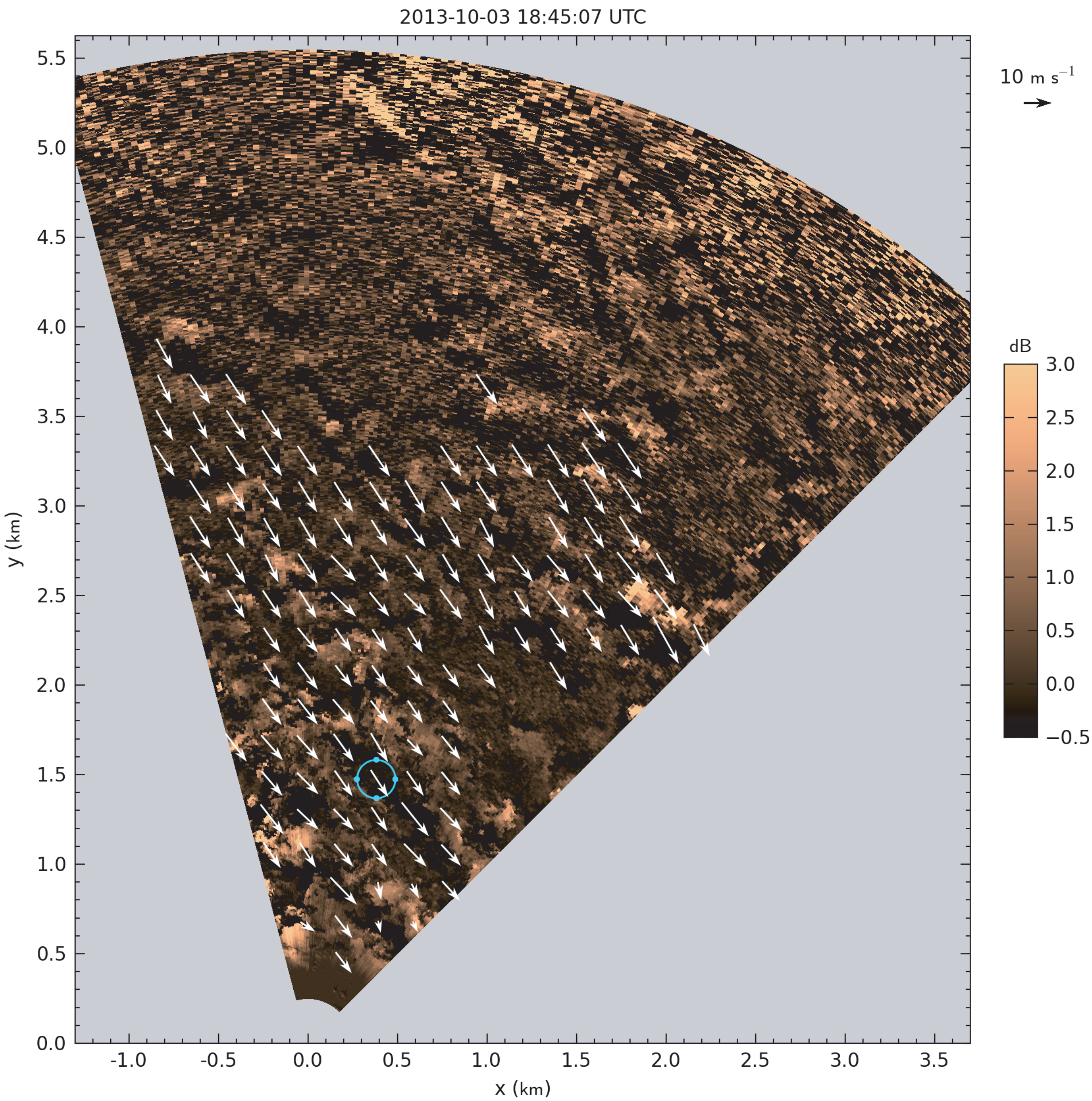

704 FIG. 13. Wind velocity field obtained by the optimized cross-correlation algorithm (3 October 2013 at
705 18:45:07 UTC), superimposed on the first scan of the pair used for estimation. The blue circle represents a
706 circular section swept by the DL.

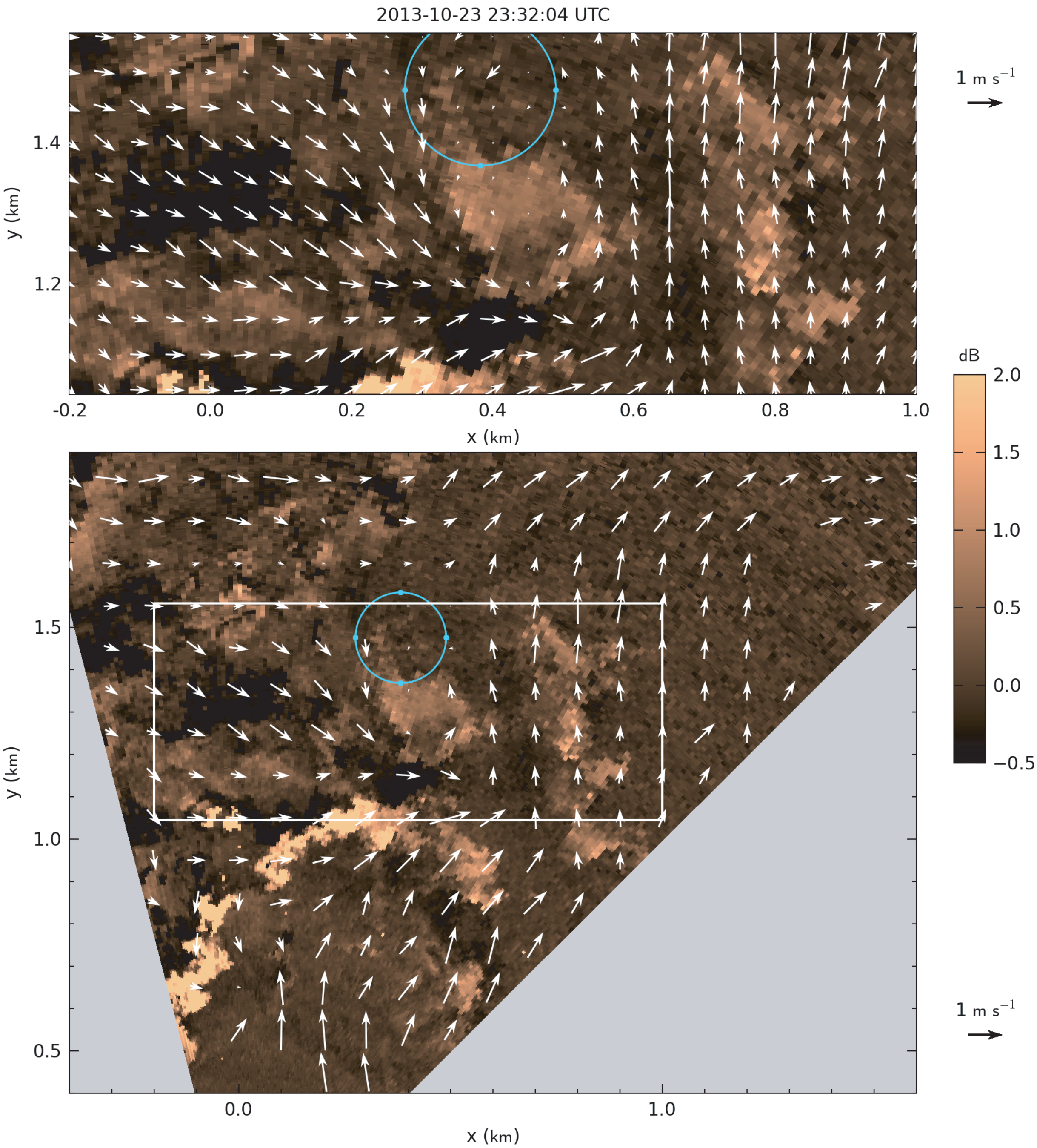

FIG. 14. Wind velocity field obtained by the optimized cross-correlation algorithm (23 October 2013 at 23:32:04 UTC), superimposed on the first scan of the pair used for estimation. The blue circle represents a circular section swept by the DL. The upper panel shows a close-up view of a vortex. The radius of the vortex is approximately 200 m.